

# Macrosegregation and Microstructural Evolution in a Pressure-Vessel Steel

E.J. Pickering and H.K.D.H. Bhadeshia

## *[Main Text]*

### Abstract

This work assesses the consequences of macrosegregation on microstructural evolution during solid-state transformations in a continuously-cooled pressure-vessel steel (SA508 Grade 3). Stark spatial variations in microstructure are observed following a simulated quench from the austenitisation temperature, which are found to deliver significant variations in hardness. Partial-transformation experiments are used to show the development of microstructure in segregated material. Evidence is presented which indicates the bulk microstructure is not one of upper bainite, as it has been described in the past, but one comprised of Widmanstätten ferrite and pockets of lower bainite. Segregation is observed on three different length scales, and the origins of each type are proposed. Suggestions are put forward for how the segregation might be minimised, and its detrimental effects suppressed by heat treatments.

### 1. Introduction

Macroscopic segregation refers to the chemical segregation which can arise over macroscopic distances during casting. In the large steel ingots used to produce pressure vessels, these distances can range from a few centimetres to a few metres. All macrosegregation originates from solidification phenomena: liquid and solid phases are either enriched or depleted in alloying elements through microsegregation, and the advection of these phases over large distances (when they move relative to one another) leads to solute being redistributed unevenly over the length scales described [1, 2]. Macroscopic segregation during the casting of large steel ingots can give rise to the defects shown in Fig. 1a. A-segregates, the particular focus of this investigation, are channels of enriched material that form along a direction roughly antiparallel to gravity during solidification. They are formed by the motion of enriched interdendritic fluid through the mushy zone, which is driven by thermosolutal convection, Fig 1b. This type of convection is not only controlled by the dissimilar temperatures of the interdendritic and bulk liquids, but also compositional disparities. In the case of steels, the interdendritic liquid will be less dense than the bulk due to the segregation of light elements like carbon and silicon, and will hence tend to rise through the mushy zone. Persistent well-defined channels of solute-rich liquid form, because as enriched liquid moves upwards and towards the centre of the casting it heats up, but does not change in composition, and so remelts the solid surrounding it (or prevents its further growth).

Any chemical inhomogeneities introduced by macrosegregation should be expected to deliver different microstructures, and hence inconsistent mechanical properties. For designers of pressure vessels such variations are highly undesirable, and yet (to the author's knowledge) investigations have not been made into how macrosegregation in pressure-vessel steels can affect microstructural evolution. Here the effects of segregation on the development of microstructure in the pressure-vessel steel SA508 Grade 3 are investigated in detail. The results of dilatometry measurements, partial-transformation experiments, and scanning and transmission electron

microscopy (SEM and TEM) are used to accomplish this. The origins of and severity of the segregation present are discussed, and suggestions are made for both how it might be prevented, and how its effects might be suppressed.

## 2. Experimental

SA508 Grade 3 material was obtained from a production component, having been cast as part of a large 200-tonne ingot before being forged, quenched and tempered. The solidification time during ingot casting was  $\sim 40$  h, and forging was carried out between 800 and 1300°C; the component was held above 1200°C for a total of over 100 h. Table 1 lists the chemical composition of the material investigated, obtained using optical emission spectroscopy, and combustion for carbon. A plate measuring  $20 \times 10 \times 2$  cm was prepared with the normal to its largest surface lying along the longitudinal direction of the ingot (i.e., pointing upwards, parallel to gravitational force). This was ground to a fine surface finish before being etched in 5% aqueous nitric acid solution, Fig. 2. Areas of positive chemical segregation were observed as dark features. By examining the material found above and below this plate, it was found the segregates extended through a significant vertical distance, indicating they were 'A' type. Cylindrical samples measuring 8 mm in diameter and 12 mm in height were taken from regions with and without A-segregation to assess their phase transformation behaviours.

A Thermecmastor\_Z dilatometer was used for monitoring the progress of phase transformations. Transformation temperatures and phase fractions were determined consistently through a linear-offset method [6]. Following dilatometry, samples were sectioned, metallographically prepared and etched in 2% nital before examination under a Lecia DM2500 M optical microscope. Chemical spot analyses were performed with a Cameca SX-100 electron probe micro analyser, whilst secondary and back-scattered electron imaging was carried out with a CamScan MX2600 field emission gun scanning electron microscope (FEGSEM). Bright-field and electron diffraction studies were undertaken in the transmission electron microscope using a JOEL 200CX machine with an accelerating voltage of 200 kV. An FEI Tecnai F20 FEG-TEM was used for Scanning TEM energy-dispersive X-ray (EDX) analysis at 200 kV. Thin foils were prepared by electropolishing with a solution of 5% perchloric acid, 25% glycerol and 70% ethanol. The voltage, current and temperature during electropolishing were 37 V, 26 mA and 10°C respectively. Vickers hardness measurements were obtained using a Mitutoyo MVK-H2 hardness testing machine, with a load of 2 kg. Prior-austenite grain size was measured by thermal etching and the linear intercept method, with data obtained from thirteen different fields of the sample and a total of 195 linear intercept lines.

## 3. Results

### 3.1. Dilatometry

Dilatometry measurements were used to characterise phase transformations during cooling from austenitisation. All samples were heated to 940°C at  $10^\circ\text{C s}^{-1}$  and held for 30 min before being cooled at  $0.1^\circ\text{C s}^{-1}$  to room temperature; the austenitisation treatment and cooling rate chosen to mimic a typical cooling rate in the middle of a thick forging during quenching. A summary of the transformation temperatures obtained from this is shown in Table 2, which also gives details of the type of transformations measured (further evidence substantiating these assignments is presented later). Fig. 3 shows examples of cooling curves from samples with and without A-

segregate material. In both cases, a transformation consistent with allotriomorphic ferrite was observed between 650 and 700°C; the fraction of ferrite and the temperature range over which it formed was greater when the austenite decomposition began at a higher temperature. The material with A-segregation showed considerably more variation in measured ferrite phase fractions, with the lowest being < 0.01 and the highest around 0.19.

The transformation event present at 550°C is associated with Widmanstätten ferrite. Fig. 3 shows that in material without A-segregation this transient was consistently reproduced and composed of two stages - the first leading to an increase in strain between 550 and 500°C and the second giving very little change in strain from 500°C until around 400°C. For samples with A-segregation, the appearance of the transformation occurring after 550°C is less consistent, although generally the first stage of transformation is not so sharp and there is more activity at lower temperatures. A comparison of typical curves for samples with and without A-segregation is seen in Fig. 4. Also shown is evidence of a low-temperature deviation in strain, which is likely to be associated with martensite formation.

### 3.2. Quenched Microstructures

Evaluation of quenched microstructures confirmed the identities of the transformations measured by dilatometry, and revealed three distinct microstructures. The first, found in the non-segregated bulk of the material, consisted of Widmanstätten ferrite, with occasional allotriomorphic grains (on prior-austenite grain boundaries), Fig. 5a. Microstructures very similar to this have previously been reported as upper bainite [7, 8, 9, 10, 11, 12], but the cleanliness of etching, the coarseness of the plates, Fig. 6a, as well as the lack of carbide precipitation (between small bainitic sub-units), Fig. 7a, suggests this is not the case.

Extensive bands of allotriomorphic ferrite formed the second distinct microstructure present. These were a few hundred µm wide and stretched for many hundreds of µm, Figs. 5b and c. They could not have resulted purely from ferrite formation on very large prior-austenite grains, as the grain size in the bulk material was found to be  $13.3 \pm 0.8 \mu\text{m}$ , and  $11.6 \pm 0.7 \mu\text{m}$  in A-segregate regions (highly non-uniform, see Fig. 8). Fine carbide precipitation was observed inside allotriomorphic grains, Fig. 7b. Electron microscopy revealed that the precipitation was not continuous, as might be expected for pearlite, Fig 7c. Orientation relationships between the cementite ( $\theta$ ) and the surrounding ferrite ( $\alpha$ ) were found to be close to the Bagaryatski relationship, Figs. 7d, e and f. This relationship is typical in tempered martensite and lower bainite, and thus suggests the carbides are part of a lower-bainite microstructure. The relationship can also be found in pearlite colonies, but is usually associated with nodules nucleated on hyper-eutectoid cementite [13, 14, 15, 16]:

Bagaryatski orientation relationship:

$$\begin{aligned} (100)_\theta &\parallel (0\bar{1}1)_\alpha \\ (010)_\theta &\parallel (1\bar{1}1)_\alpha \\ (001)_\theta &\parallel (211)_\alpha \end{aligned}$$

The third microstructure present was that found in regions enriched in solute by A-segregation, which were found to be darker and more finely-structured than the Widmanstätten bulk in optical micrographs, Fig. 5d. Blocky regions of material, which had not been readily etched, were identified under the SEM, Fig. 6c, and were particularly prominent in back-scattered electron

images, Fig. 6d, indicating enrichment in heavy elements and/or a difference in phase. TEM revealed that these regions were composed of retained austenite, Figs. 9a and b, and that in some cases this had decomposed into martensite, Fig. 9c. These martensite-austenite islands were also occasionally found in the bulk Widmanstätten and allotriomorphic ferrite microstructures, as highlighted in Figs 6a and b.

Elsewhere in A-segregate material, lower bainite appeared to be the most common microstructure between the martensite-austenite islands, Fig. 10a, along with some Widmanstätten ferrite. An orientation relationship consistent with Bagaryatski was found in the lower bainite regions, and the fine platelets of lower bainite were readily distinguished, Fig. 10b. In addition to cementite precipitation, distinctive globular/near spherical carbides were also observed, Fig. 10c. Bright-field imaging, diffraction and STEM EDX suggested that they were  $M_6C$  particles that had formed during the slow cooling from austenitisation. There was no evidence of their presence in non-enriched material.

Small globular MnS and mixed-oxide inclusions (with large dimension not greater than 30  $\mu\text{m}$ , and more commonly far smaller) were sparsely distributed in a random fashion throughout all material examined, with a number density of  $< 30 \text{ mm}^{-2}$  for sizes of 2 - 30  $\mu\text{m}$ . In addition, larger MnS inclusions were occasionally found in enriched A-segregate material, Fig. 10d, and often appeared elongated in the forging direction. The number density of inclusions with largest dimension  $> 40 \mu\text{m}$  was  $\sim 0.2 \text{ mm}^{-2}$  within the channels examined.

### **3.3. Tempered Microstructures**

Following the simulated quenching heat-treatment, samples were tempered 645°C for 6 h with heating and cooling rates controlled at 30°C h<sup>-1</sup> to simulate conditions at the middle of a thick section. This led to the coarsening of cementite, Fig. 11, particularly so in the A-segregate material where  $\text{Mo}_2\text{C}$  also precipitated, Fig 12 ( $\text{Mo}_2\text{C}$ ). The martensite-austenite islands decomposed into a ferrite/cementite mixture, but these regions were still more resistant to etchant attack, as highlighted in Figs. 11c and d.

### **3.4. Chemistry**

The three microstructurally-distinct regions discovered in as-quenched material were subjected to electron-probe broad-beam spot-analysis, Table 3. The results are consistent with the microstructural observations that indicate a much greater hardenability and propensity to precipitate carbides, within the A-segregated regions, which are significantly enriched with respect to manganese, nickel and molybdenum.

### **3.5. Hardness**

Vicker's hardness measurements were taken from three distinct regions in as-quenched and as-tempered material: (i) the bands of allotriomorphic ferrite, (ii) the bulk matrix (Widmanstätten ferrite) and (iii) A-segregate regions. Measurements of (i) and (ii) were taken from all samples, whilst measurements of (iii) could only be taken from samples containing A-segregates. Results, given in Table 4, show a significant variation in hardness between the three regions after quenching, but that tempering suppresses the variations and leads to general softening. The size

of indentations in as-quenched material ranged from  $\sim 150 \mu\text{m}$  across in regions rich in allotriomorphic ferrite to  $\sim 100 \mu\text{m}$  in A-segregate material.

### 3.6. Partial-Transformation Experiments

The simulated quench was interrupted at various stages by cooling at  $25^\circ\text{C s}^{-1}$  in order to follow the development of microstructure, as illustrate in Fig. 4. The images in Fig. 13 are from regions not containing any A-segregation; allotriomorphic ferrite dominates above  $600^\circ\text{C}$ , and the transformation beginning at  $550^\circ\text{C}$  is associated with the formation of both primary and secondary Widmanstätten ferrite. The transformation of carbon-enriched regions between Widmanstätten and allotriomorphic grains occurred  $\sim 500\text{--}400^\circ\text{C}$ , with the formation of cementite associated with the relatively flat dilatational response over this temperature range. Some austenite remained untransformed at  $400^\circ\text{C}$ , as highlighted in Fig. 13d, and it is likely that some will be retained to lower temperatures. In contrast, the A-segregated regions (Fig. 14) remained untransformed until about  $600^\circ\text{C}$ , with little Widmanstätten ferrite prior to about  $500^\circ\text{C}$  (except where depleted, allotriomorphic ferrite-rich bands stretched into segregated regions, Fig. 5c). The formation of more bainite at lower temperatures, with finer carbide precipitation, appears to have led to the greater change in dilatation  $400^\circ\text{C}$ .

## 4. Discussion

Homogeneous mechanical properties are obviously desirable for pressure vessels, and the segregation associated with the solidification of large ingots makes this unlikely [17, 18, 19, 20, 21]. For instance, toughness is the most important property for pressure-vessel steels, and it very likely that the significant scatter observed in toughness measurements [22, 23, 24, 25] is in part due to segregation effects [20, 21]. Scatter in all mechanical property data adds to uncertainty in the assessment of structural integrity, so the discussion below is intended to highlight the consequences of chemical segregation and suggest possible remedies.

### 4.1. Evolution of Microstructure and Hardness

The observed transformation sequences can be summarised as follows. In the bulk non-segregated material, allotriomorphic ferrite first nucleates at grain boundaries followed by the formation of Widmanstätten ferrite starting at around  $550^\circ\text{C}$ . Carbon is partitioned into the residual austenite as ferrite grows, and the enriched austenite then transforms into lower bainite incorporating coarse carbides. The lack of well-defined fine platelets in this bainite, as well as the coarseness of the carbides, is likely due to a combination of the relatively high temperature of transformation, and the slow cooling rate. The A-segregated regions have sufficient hardenability to avoid allotriomorphic ferrite, and contain only a limited amount of Widmanstätten ferrite, transforming instead to a predominantly lower bainitic microstructure with a residue of martensite-austenite islands.

As-quenched hardness values are consistent with the observed microstructures, Table 4. Coarse allotriomorphic ferrite is softest, with the finer plates of Widmanstätten ferrite being a little harder. The fine structure of lower bainite and martensite-austenite islands gave a much higher hardness to A-segregated material. Tempering naturally led to a general reduction in hardness, particularly in the segregated regions where the decomposition of the martensite-austenite is-

lands significantly reduced the hardness in spite of the precipitation of Mo<sub>2</sub>C particles.

Available literature on the subject of impact toughness in SA508 Grade 3 suggests that A-segregate material is likely to be significantly less tough than the bulk, particularly at low temperatures. It is true that, based on the scale of the microstructure and carbide precipitation, segregated material might be expected to be tougher: finer, harder microstructures have generally been found to be tougher in SA508 Grade 3 [11, 24, 26, 27], hence tempered martensite is preferred, and it seems plausible that the regions of coarse lower-bainitic carbides present between Widmanstätten laths in the bulk could preferentially promote crack nucleation [7, 10, 11, 26]. However, this ignores the segregation of embrittling species like S and P to A-segregate material. The results of investigations in which the impact toughness of A-segregate material has been specifically targeted have universally found a significant decrease in impact toughness compared to the bulk, both in the upper and lower-shelf regimes [18, 20, 21, 28]. A number of studies have suggested that the lower upper-shelf impact energies can be attributed to higher levels of coarse MnS particles within enriched material [18, 28], whilst it seems that decreased lower-shelf impact values are often associated with intergranular failure due to P embrittlement of prior-austenite grain boundaries [20, 21, 29]. An ongoing investigation by the author has found further evidence of intergranular failure in SA508 Grade 3 A-segregate material, Fig. 15, and is seeking to confirm its origin through the use highly-sensitive chemical analysis, the results of which will be presented at a later date. The effect of segregation as a contributor to the wide scatter that can be observed in Charpy results around the ductile-to-brittle transition will also be discussed.

On a coarser scale, microsegregation during solidification leads to the bands of allotriomorphic ferrite at the cores of dendrites, illustrated in Fig. 16, which shows a partially transformed sample at a scale consistent with expected primary and secondary dendrite arm spacings in large ingots [30, 31, 32, 33, 34]. It is likely that the scatter in the amount of allotriomorphic ferrite detected, particularly in samples with A-segregates, is due to the probabilistic nature of finding dendrite-arm cores within a sample. Banding of this kind is well known, and is determined not only by solute concentrations but also the heat treatment applied [35, 36, 37, 38, 39, 40]; unlike conventional banding in wrought steels, deformation plays very little role in the nature of the bands observed here. The microstructural banding observed in wrought-steels can be mitigated by increasing the austenite grain size or the cooling rate from austenitisation [35, 36, 37, 38, 39, 40]. The former is undesirable in that it could lead to a decrease in toughness through increased boundary embrittlement and coarser transformation products. A recent study suggests that cooling rates of 0.2 or 0.4°C s<sup>-1</sup> are sufficient to suppress allotriomorphic ferrite formation in SA508 Grade 3 [41], and so this was investigated as a remedial method. These cooling rates led to the development of microstructures which were similar to those formed at 0.1°C s<sup>-1</sup>, Fig. 17, although they were free of allotriomorphic ferrite bands, appeared finer, and contained more martensite-austenite islands. A finer microstructure is expected to be tougher if it leads to finer cementite precipitation, and higher cooling rates are often sought in thick sections for this reason. The hardnesses obtained from these samples were not significantly different to the original condition, however, suggesting that the scale of the microstructure had not changed remarkably, Table 5. Thus it seems that increasing cooling rates from austenitisation can effectively mitigate the effects of residual microsegregation and would likely only improve bulk toughness through a finer microstructure. Increasing the mid-thickness cooling rate of a large forging to the required level in a commercial setting would, of course, be difficult due to conduction-limited cooling rates.

## 4.2. Macrosegregation Prediction

The final segregation mechanism at work in the material examined was macrosegregation, specifically A-segregation. In pressure vessels the impingement of A-segregates on weld areas is a particular concern, and it would be useful to predict their composition and location as well as minimise their formation. The results of an EPMA linescan between two dendrite arms which protruded into a segregate channel is shown in Fig. 18. One might expect that the concentration of liquid contained within a channel segregate would lie somewhere between the limiting lever-rule (equilibrium) and Scheil (non-equilibrium) cases, and that the concentrations of each element would be consistent with a certain point in solidification in a given microsegregation model, e.g., a fraction solid of 0.7. However, a comparison of the measured data and MTDATA equilibrium and Scheil calculations shows that this is unlikely to be true if current microsegregation models [42, 43, 44, 45] are used with typical partition coefficients between liquid and solid, Table 6 (the partition coefficients used here were calculated in MTDATA, but similar values can be found in standard binary phase diagrams and other texts [46, 47]). It is clear that some species are enriched far beyond the equilibrium limit (Cr and Ni), whilst others retain lower concentrations (Mo, Mn, Si). It is true that the diffusion of species over long periods of time during forging might have led to a higher level of Ni and lower level of Si relative to the other elements (they are significantly slower and faster diffusers, respectively), but the enrichment of Cr cannot be accounted for in this way. Thus, it is highly unlikely that the A-segregate liquid retained a composition which can be shown to be consistent with a particular stage of solidification in any commonly-available microsegregation models, certainly not the equilibrium lever-rule scheme. Further work will seek to examine A-segregate enrichment in an as-cast product, where complicating factors such as heat treatment and forging are not present.

Investigations into the prediction of the location of A-segregates are currently ongoing, utilising the Rayleigh number of Torabi Rad, Beckermann et al. [48] in the same large-scale casting trials. What is already apparent, however, is that by making adjustments to the composition of SA508 Grade 3 and other alloys within their specifications [49], the driving force for interdendritic fluid flow could be reduced leading to less A-segregation. Previous studies have indicated this should be possible by decreasing the Si and increasing the Mo content of low-alloy steels [48, 50, 51, 52]. Indeed, it has been suggested that this not only reduces the buoyancy differences driving fluid flow, but also decreases the permeability of the mushy zone by changing the dendrite spacing and morphology [51, 52, 53]. A less permeable mushy zone may lead to increased porosity (although this may be negated by a decreased freezing range), and that increased Mo and decreased Si levels will lead to a higher liquid viscosity and hence higher inclusion retention levels. The effect of compositional change on microstructural and mechanical properties should also be explored fully before a change in chemistry implemented. Nevertheless, for SA508 Grade 3 there are a number of reasons for why this change may prove to be beneficial. Si is added to the alloy for deoxidation purposes, but there are alternative methods for deoxidation and improved modern steelmaking processes mean this addition is not an essential as it has been in the past. Furthermore, decreasing Si content has been associated with better impact properties [52] and its hardening effect is easily accounted for by increasing Mo. Adding more Mo has been shown to encourage the growth of more  $\text{Mo}_2\text{C}$  in competition with  $\text{Fe}_3\text{C}$ , reducing the volume fraction of coarse cementite particles, improving mechanical properties and reducing the ductile-to-brittle transition temperature without adverse irradiation effects [7, 8, 9, 11, 54, 55]. This may also allow for a lower carbon content, which will similarly reduce macrosegregation and the precipitation of coarse carbides. Increased microsegregation of Mo could be a potential problem, but if dendrite arm spacings are decreased by the composition changes then this may be less of an issue.

## 5. Summary and Conclusions

1. Simulated quenching of segregated SA508 Grade 3 material led to appreciable spatial variations in microstructure. In regions enriched in solute, a microstructure of Widmanstätten ferrite, lower bainite and martensite-austenite islands was found, whilst depleted areas at the former-dendrite arm centres, saw extensive allotriomorphic ferrite formation.
2. The bulk microstructure was found to be predominantly Widmanstätten ferrite, contrary to previous reports of microstructure, where it has been classified as upper bainite. Regions between Widmanstätten and allotriomorphic ferrite grains, which had been enriched in carbon during transformation, were found to contain lower bainite with coarse cementite particles.
3. The hardness of as-quenched and tempered material varied significantly with the microstructure. The toughness is expected to be influenced by these variations and further investigations are ongoing.
4. The extensive allotriomorphic ferrite bands observed in the microstructure were a result of solidification-induced segregation. It was found that increasing the cooling rate allowed these bands to be eliminated.
5. The concentration of A-segregate liquid was found to be inconsistent with current microsegregation models and partition coefficients. It is suggested that the formation of A-segregates could be reduced by decreasing the Si content and increasing the Mo content of SA508 Grade 3, and that this may improve mechanical properties. Large-scale casting trials are ongoing which aim to characterise A-segregates more closely.

## Acknowledgements

This work was undertaken as part of a project sponsored by Rolls-Royce Power Engineering plc in collaboration with Sheffield Forgemasters International. We extend our thanks to Professor Lindsay Greer for provision of lab facilities and electron microscopes. The author would like to thank D. Cogswell, S. Ooi and H. Pous-Romero for helpful discussions.

## References

- [1]. J.A. Dantzig and M. Rappaz: *Solidification*, EPFL Press, 2009.
- [2]. E.J. Pickering: *ISIJ*, 2013, vol. 53, pp. 935-949.
- [3]. M.C. Flemings: *Solidification Processing*, McGraw-Hill, January 1974.
- [4]. H.F. Taylor, M.C. Flemings, and J. Wulff: *Foundry Engineering*, Wiley, New York, 1959.
- [5]. E. Marburg: *JOM*, 1953, vol. 2, pp. 157–172.
- [6]. H-S. Yang and H.K.D.H. Bhadeshia: *Mater. Sci. Tech.*, 2007, vol. 23, pp. 556–560.

- [7]. Y.R. Im, Y.J. Oh, B.J. Lee, J.H. Hong, and H.C. Lee: *J. Nucl. Mater.*, 2001, vol. 297, pp. 138–148.
- [8]. S. Kim, Y.R. Im, S. Lee, H.C. Lee, Y.J. Oh, and J.H. Hong: *Metall. Mater. Trans. A*, 2001, vol. 32A, pp. 903–911.
- [9]. S. Lee, S. Kim, B. Hwang, B.S. Lee, and C.G. Lee: *Acta Mater.*, 2002, vol. 50, pp. 4755–4762.
- [10]. Y.R. Im, B.J. Lee, Y.J. Oh, J.H. Hong, and H.C. Lee: *J. Nucl. Mater.*, 2004, vol. 324, pp. 33–40.
- [11]. S. Kim, S. Lee, Y.R. Im, H.C. Lee, S.J. Kim, and J.H. Hong: *Metall. Mater. Trans. A*, 2004, vol. 35A, pp. 2027–2037.
- [12]. B.S. Lee, M.C. Kim, J.H. Yoon, and J.H. Hong: *Int. J. Press. Ves. Pip.*, 2010, vol. 87, pp. 74–80.
- [13]. Y. Bagaryatski: *Dokl. Akad. Nauk. SSSR*, 1950, vol. 73, pp. 1161.
- [14]. D.N. Shackleton and P.M. Kelly: *Acta Metall.*, 15:979–992, 1967.
- [15]. H.K.D.H. Bhadeshia: *Bainite in Steels*, The Institute of Materials, 1992.
- [16]. H.K.D.H. Bhadeshia and R.W.K. Honeycombe: *Steels: Microstructure and Properties*, 3rd edition, Butterworth-Heinemann, 2006.
- [17]. Heterogeneity Sub-Committee of the British Iron and Steel Institute: *JISI*, 1926, vol. 113, pp. 39–151.
- [18]. S.G. Druce: AERE report R9581, Harwell, September 1979.
- [19]. G. Ostberg: *Int. J. Press. Ves. Pip.*, 1997, vol. 74, pp. 153–158.
- [20]. A-A Tavassoli, P. Soulat, and A. Pineau: *Residual and Unspecified Elements in Steel*, ASTM STP 1042, pp. 100–113, ASTM, Philadelphia, 1989.
- [21]. P. Soulat, B. Houssin, P. Bocquet, and M. Bethmont: *Radiation Embrittlement of Nuclear Reactor Pressure Vessel Steels: An International Review*, pp. 249–265, ASTM, 1993.
- [22]. B.S. Lee, J.H. Hong, W.J. Yang, M.Y. Huh, and S.H. Chi: *Int. J. Press. Ves. Pip.*, 2000, vol. 77, pp. 599–604.
- [23]. F.M. Beremin: *Metall. Trans. A*, 1984, vol. 14A, pp. 2277–2287.
- [24]. J.T. Kim, H.K. Kwon, H.S. Chang, and Y.W. Park: *Nucl. Eng. Des.*, 1997, vol. 174, pp. 51–58.
- [25]. K.H. Lee, M.C. Kim, B.S. Lee, and D.M. Wee: *J. Nucl. Mater.*, 2010, vol. 403, pp. 68–74.

- [26]. P. Bowen, S.G. Druce, and J.F. Knott: *Acta Metall.*, 1986, vol. 34, pp. 1121–1131.
- [27]. K.D. Haverkamp, K. Forch, K.H. Piehl, and W. White: *Nucl. Eng. Des.*, 1984, vol. 81, pp. 207–217.
- [28] C. Maidorn and B. Blind: *Nucl. Eng. Des.*, 1985, vol. 84, pp. 285–296.
- [29]. C. Naudin, J.M. Frund, and A. Pineau: *Scripta Mater.*, 1999, vol. 40, pp. 1013–1019.
- [30]. A. Suzuki, T. Suzuki, Y. Nagaoka, and Y. Iwata: *Nippon Kingaku Gakkai Shuho*, 1968, vol. 32, pp. 1301–1305.
- [31]. H. Jacobi and K. Schwerdtfeger: *Metall. Trans. A*, 1976, vol. 7A, pp. 811–820.
- [32]. M. El-Bealy and H. Fredriksson: *Metall. Mater. Trans. B*, 1996, vol. 27B, pp. 999–1014.
- [33]. Y.M. Won and B.G. Thomas: *Metall. Mater. Trans. B*, 2001, vol. 32A, pp. 1755–1767.
- [34]. T.Z. Kattamis, J.C. Coughlin, and M. C. Flemings: *Trans. Metall. Soc. AIME*, 1967, vol. 239, pp. 1504–1511.
- [35]. P.G. Bastien: *J. Iron Steel I.*, 1957, vol. 187, pp. 281–291.
- [36]. J.S. Kirkaldy, J. von Destinon-Forstmann and R.J. Brigham: *Can. Metall. Q.*, 1962, vol. 1, pp. 59–81.
- [37]. L.E. Samuels: *Optical Microscopy of Carbon Steels*, ASM, 1980.
- [38]. S.W. Thompson and P.R. Howell, *Mat. Sci. Tech.*, 1992, vol. 8, pp. 777–784.
- [39]. R. Grossterlinden, R. Kawalla, U. Lotter and H. Pircher: *Steel Res.*, 1992, vol. 63, pp. 331–336.
- [40]. J.D. Verhoeven: *J. Mater. Eng. Perform*, 2000, vol. 9, pp. 286–296.
- [41]. H. Pous-Romero: Ph.D. Thesis, University of Cambridge, UK, 2014.
- [42]. E. Scheil. Bemerkungen zur Schichtkristallbildung: *Ziets. Metall.*, 1942, vol. 34, pp. 70.
- [43]. T.W. Clyne and W. Kurz: *Metall. Trans. A*, 1981, vol. 12A, pp. 965–971.
- [44]. T. Ohnaka: *Tetsu To Hagane*, 1984, vol. 70, pp. S913.
- [45]. V.R. Voller and C. Beckermann: *Metall. Mater. Trans. A*, 1999, vol. 30A, pp. 2183–2189.
- [46]. T.B. Massalski, H. Okamoto, P.R. Subramanian and L. Kacprzak (eds.): *Binary Alloy Phase Diagrams, Volume 2*, 2nd edition, ASM International, 1990.
- [47]. Physical Chemistry of Steelmaking Committee: *Basic Open Hearth Steelmaking*, 3rd edition, AIME, 1964.

- [48]. M. Torabi, P. Kotas, and C. Beckermann: *Metall. Mater. Trans. A*, 2013, vol. 44A, pp. 4266-4281.
- [49]. ASTM Standard Specification for Quenched and Tempered Vacuum-treated Carbon and Alloy Steel Forgings for Pressure Vessel Components A508A/A548M, 2004.
- [50]. C.E. Smeltzer: *Iron Age*, 1959, vol. 184, pp. 188-189.
- [51]. K. Suzuki and K. Taniguchi: *Transactions ISIJ*, 1981, vol. 21, pp. 235–242.
- [52]. S. Kawaguchi, H. Tsukada, K. Suzuki, I. Sato, M. Kusuhashi, and S. Onodera: *Nucl. Eng. Des.*, 1985, vol. 87, pp. 249–257.
- [53]. K. Suzuki and T. Miyamoto: *Trans. ISIJ*, 1980, vol. 20, pp. 377–383.
- [54]. B. Tanguy, J. Besson, and A. Pineau: *Scripta Mater.*, 2003, vol. 49, pp. 191–197.
- [55]. J.R. Hawthorne: *Nucl. Eng. Des.*, 1985, vol. 89, pp. 223–232.

**[Figures]**

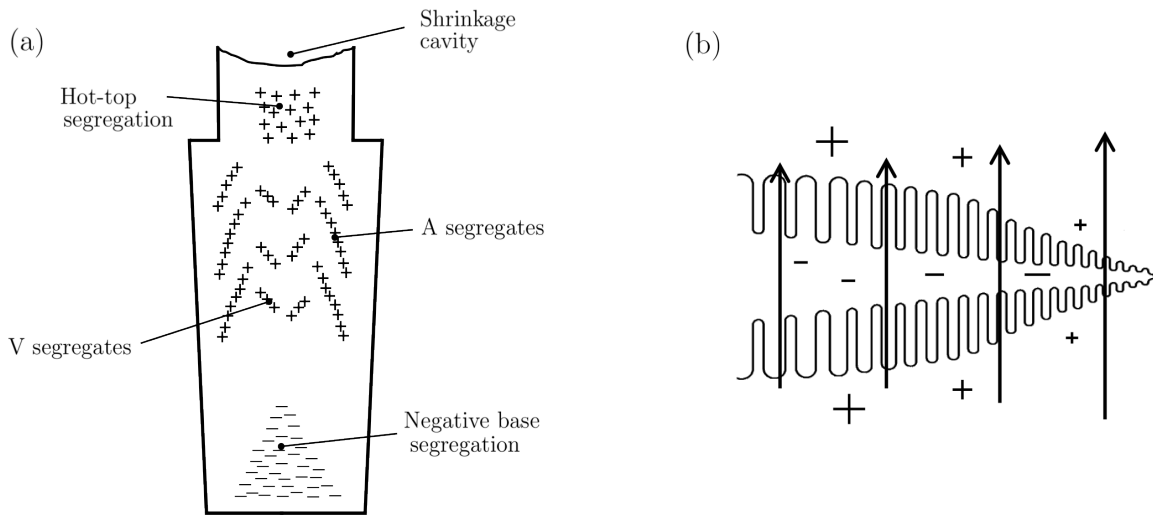
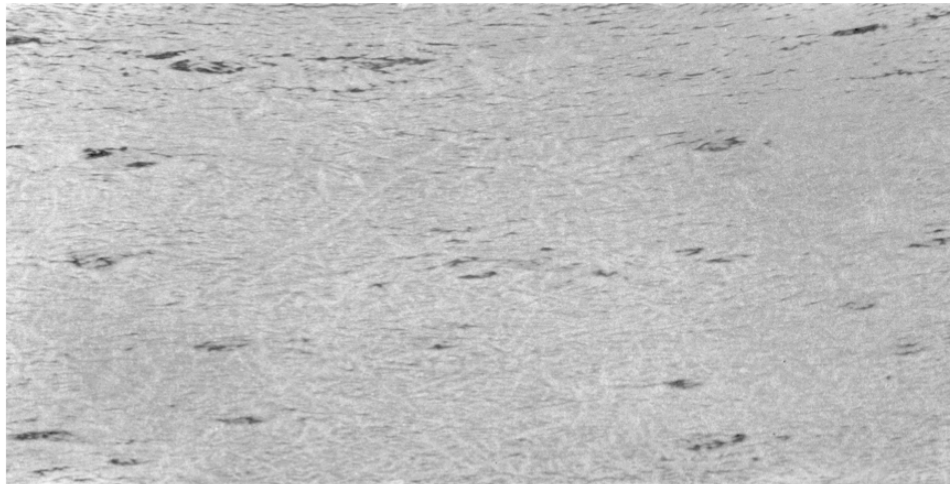


Figure 1: (a). Different types of macrosegregation typically found in large ingots. Positive segregation is denoted by + symbols representing regions enriched in solute, and negative by – for solute-depleted regions. Similar figures can be found in [3, 4, 5]. (b). Schematic of interdendritic fluid flow driven by thermosolutal convection. This flow leads to the formation of A-segregates.



2 cm

Figure 2: Section of SA508 Grade 3 forging, metallographically prepared and macroetched. Dark regions are areas of positive segregation. In this view, the upward direction points towards the ingot centre. A becking forging operation (similar ring forging) has elongated the segregates tangentially.

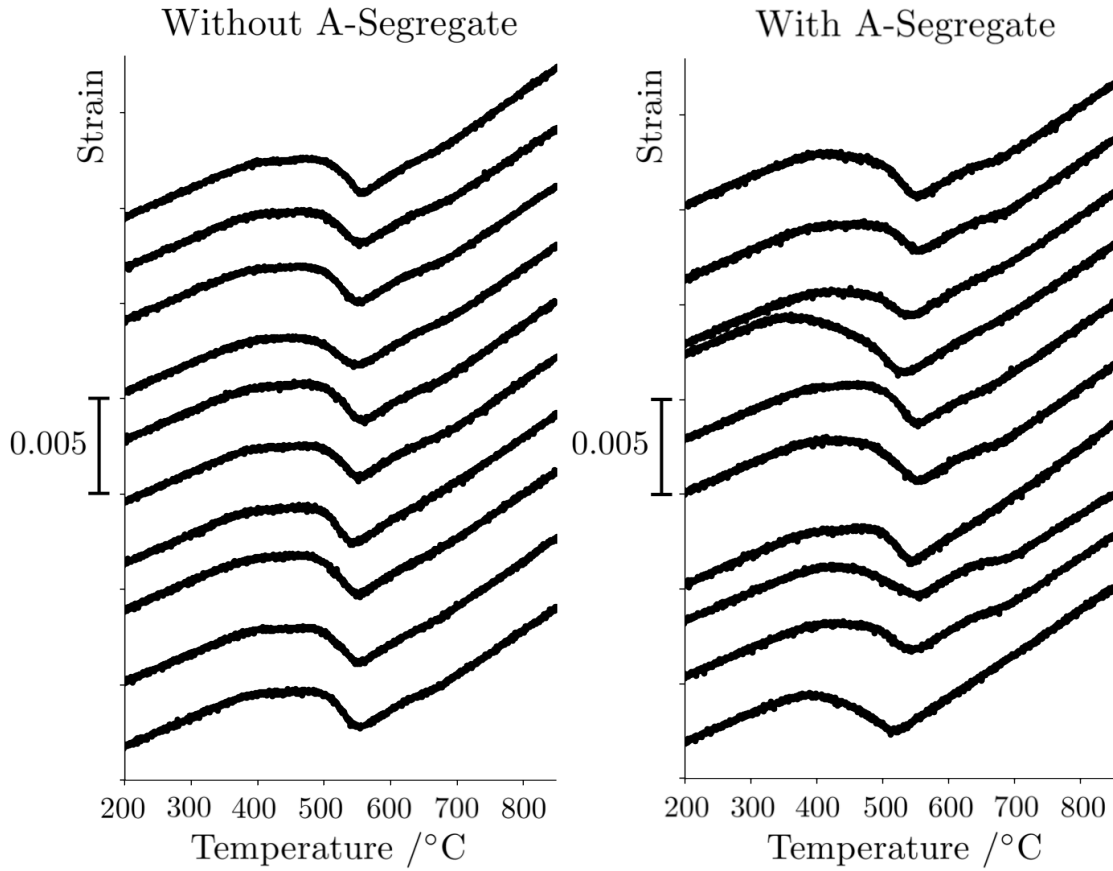


Figure 3: Comparison of strain curves for samples with and without A-segregation. Those without A-segregation display more consistent behaviour than those with.

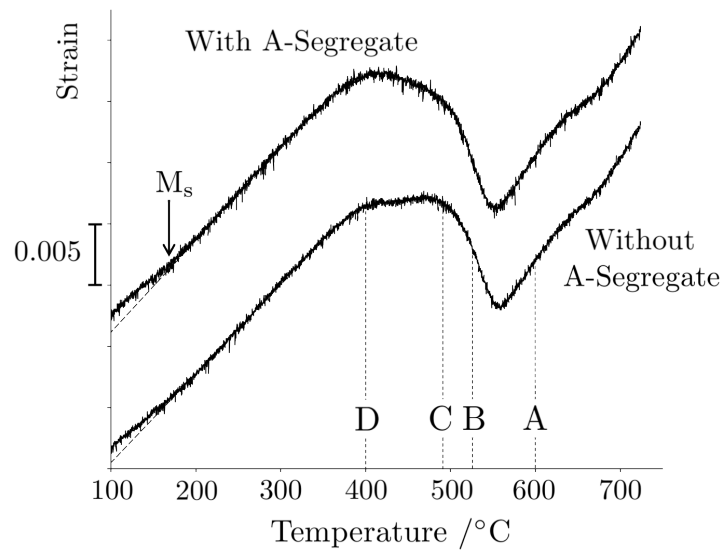


Figure 4: Comparison of typical strain curves for material with and without A-segregation. There

is evidence of more low-temperature transformation in samples with A-segregation. The points labelled A, B, C and D refer to the temperatures at which the material was quenched during partial transformation experiments. Martensite start temperatures are also highlighted ( $M_s$ ).

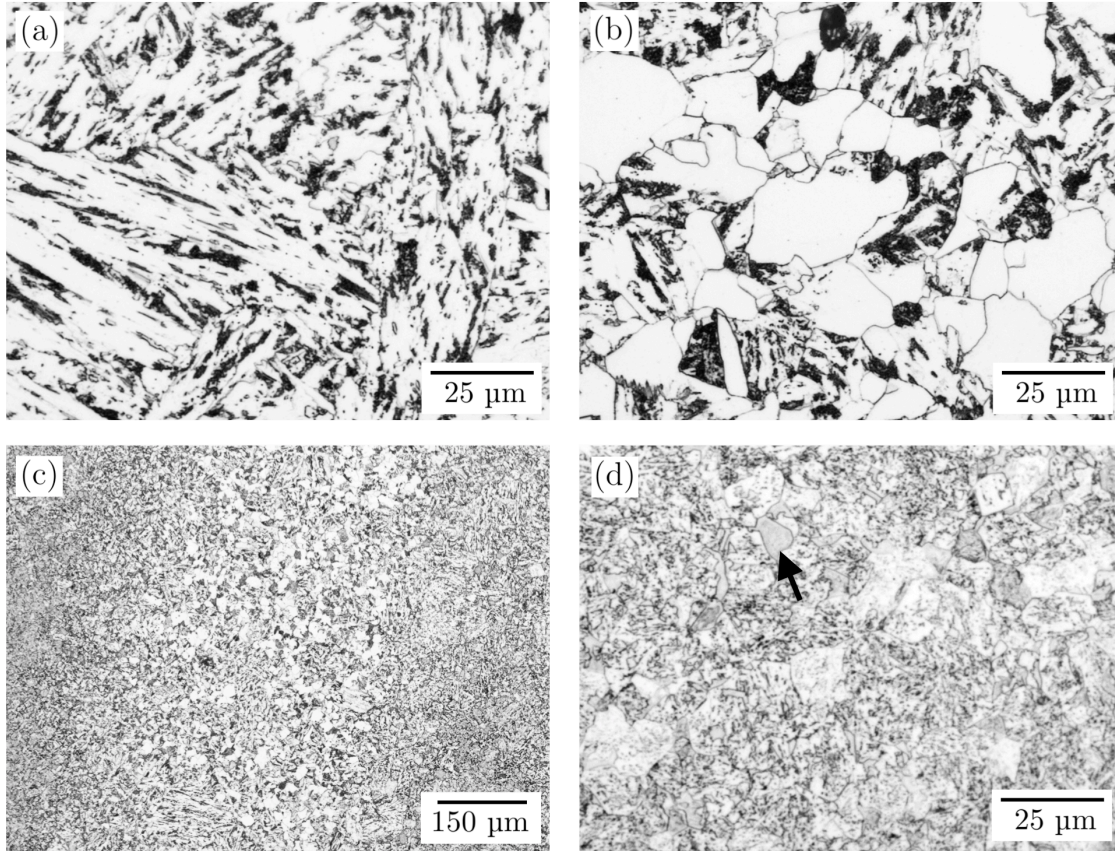


Figure 5: Optical microscopy of as-quenched material. (a) the Widmanstätten ferrite bulk. (b) inside allotriomorphic ferrite bands. (c) allotriomorphic ferrite band inside enriched A-segregate material. (d) A-segregate material, with martensite-austenite island highlighted.

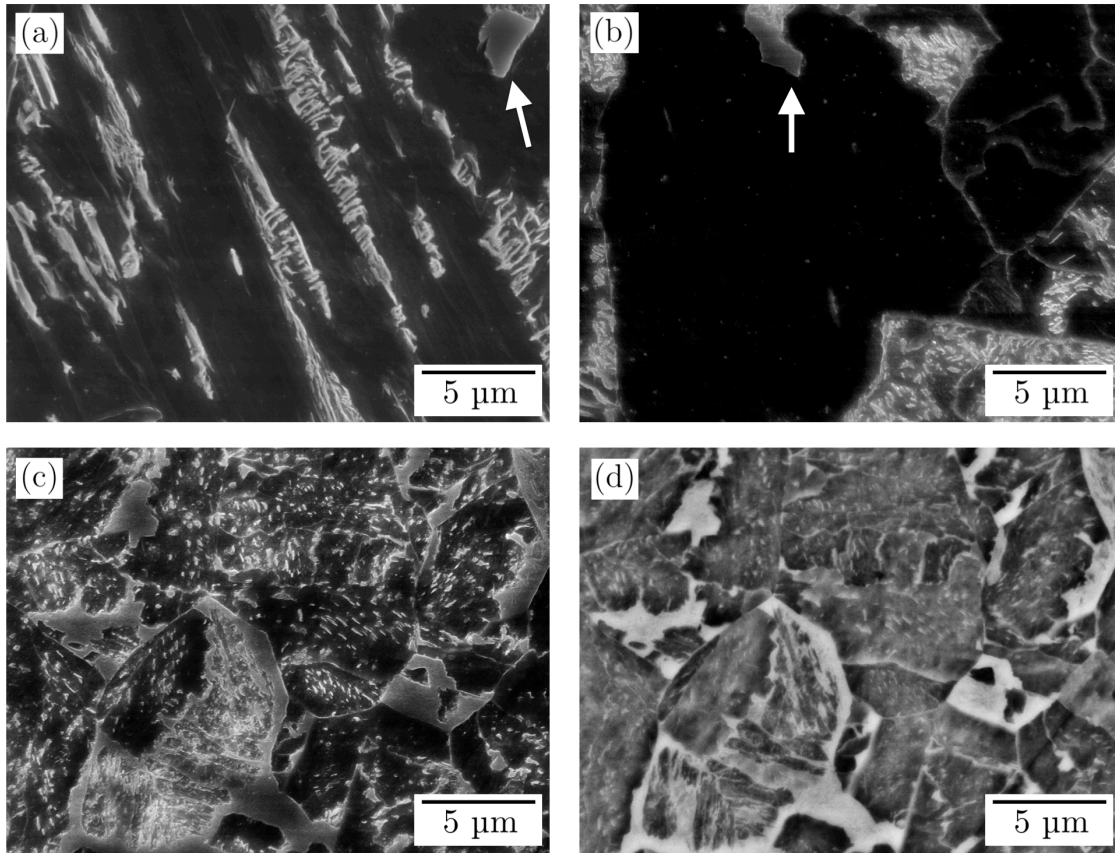


Figure 6: Secondary-electron micrographs of the Widmanstätten bulk, allotriomorphic regions and enriched regions are shown in (a), (b) and (c) respectively. Martensite-austenite islands are highlighted. (d) shows a back-scattered electron image of the enriched material in (c), with increased electron yield from martensite-austenite islands.

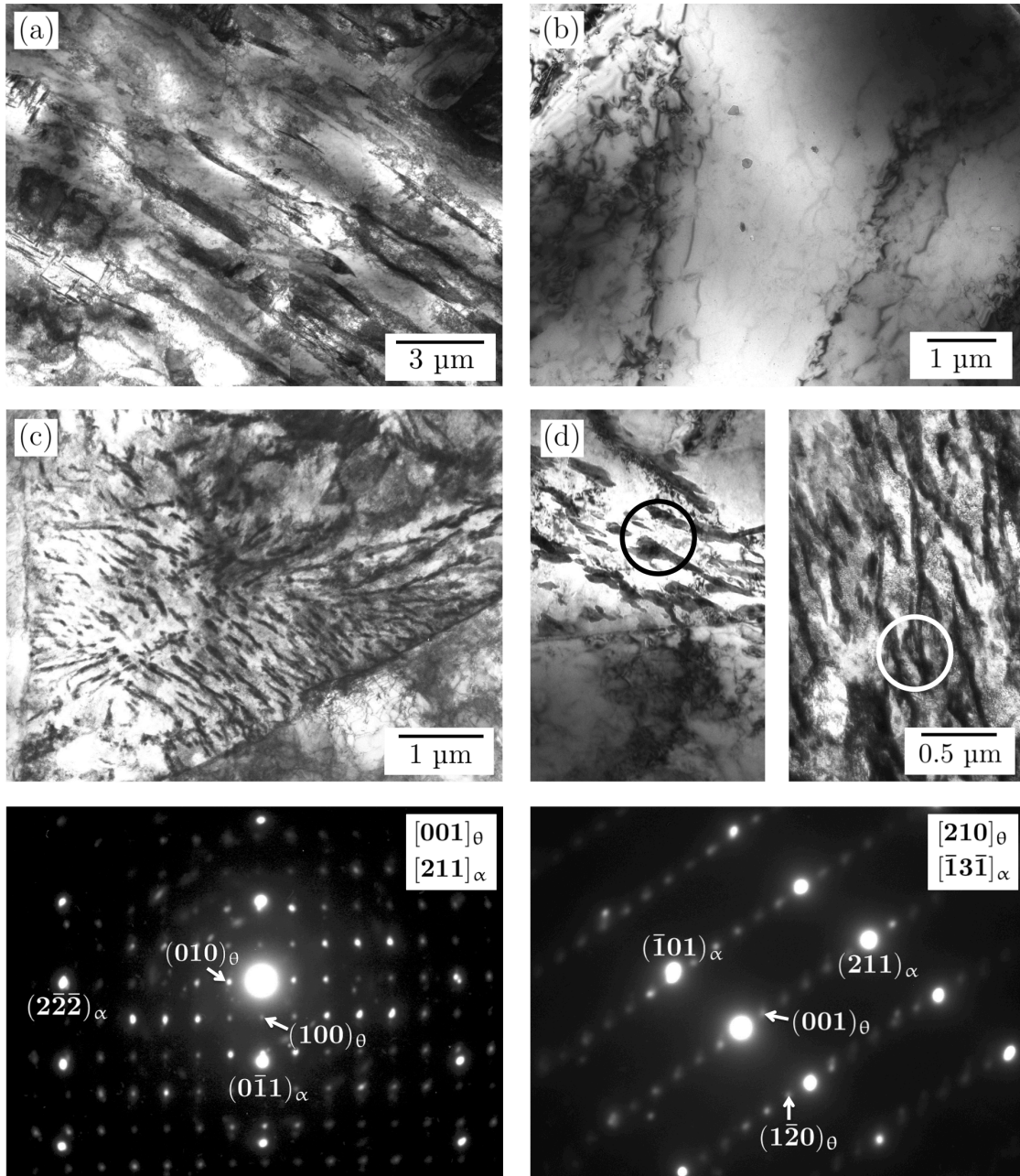


Figure 7: TEM bright-field imaging and diffraction. (a) Coarse Widmanstätten ferrite laths with no inter- or intra-lath cementite precipitation. (b) Fine carbide precipitation found within allotriomorphic grains. (c) and (d) show inter-ferrite cementite-rich regions. The electron diffraction patterns in (e) and (f), obtained from the left and right regions highlighted in (d) respectively, confirm cementite and the Bagaryatski orientation.

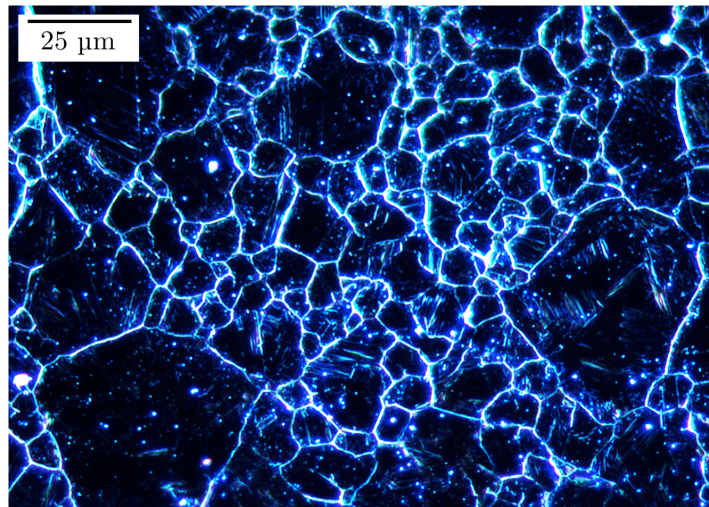


Figure 8: Prior-austenite grain structure, exhibiting a non-uniform grain size. Micrograph obtained by thermal etching, and dark-field optical microscopy.

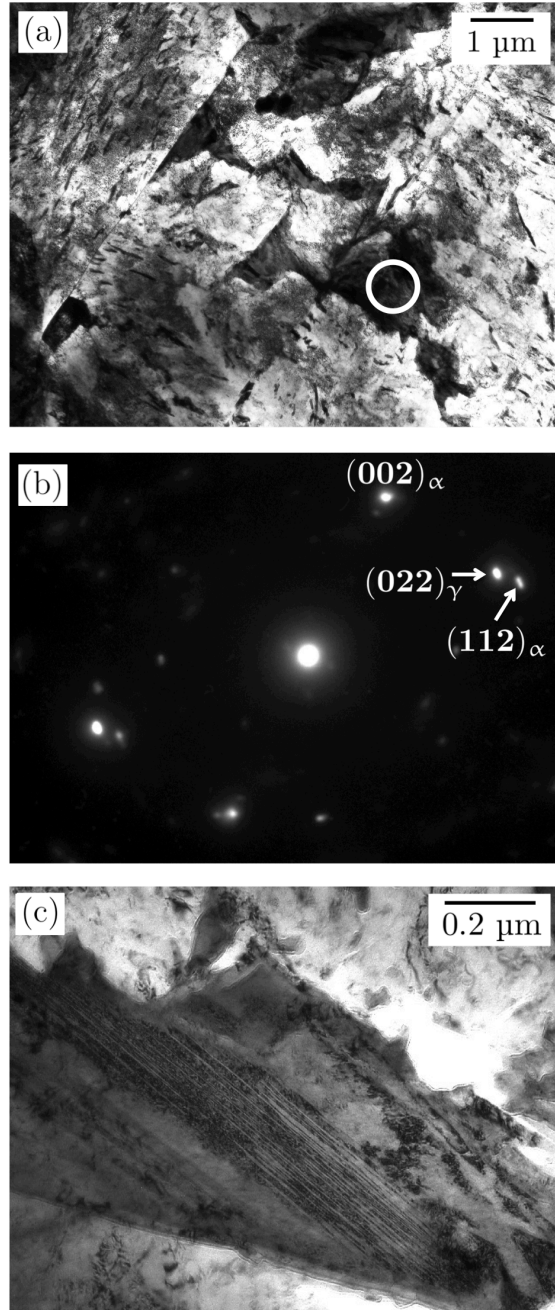


Figure 9: Martensite-austenite islands. (a) Islands at prior-austenite grain boundaries. (b) Electron diffraction analysis of the area highlighted in (a). (c) High-carbon twinned martensite within the islands.

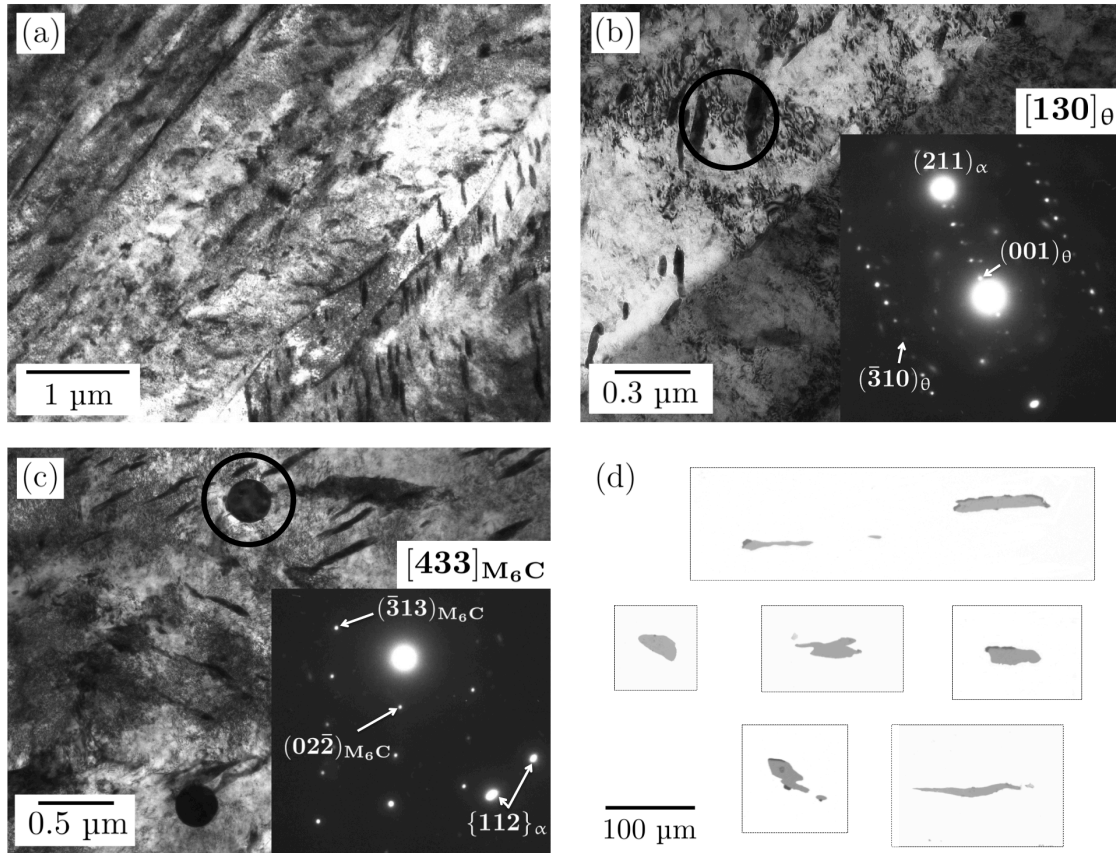


Figure 10: A-segregate region. (a) and (b) show TEM images and diffraction analysis consistent with lower bainite. (c)  $M_6C$  precipitates found exclusively in A-segregates. (d) Optical images of the larger MnS inclusions, with each box representing a different area of sampled material.

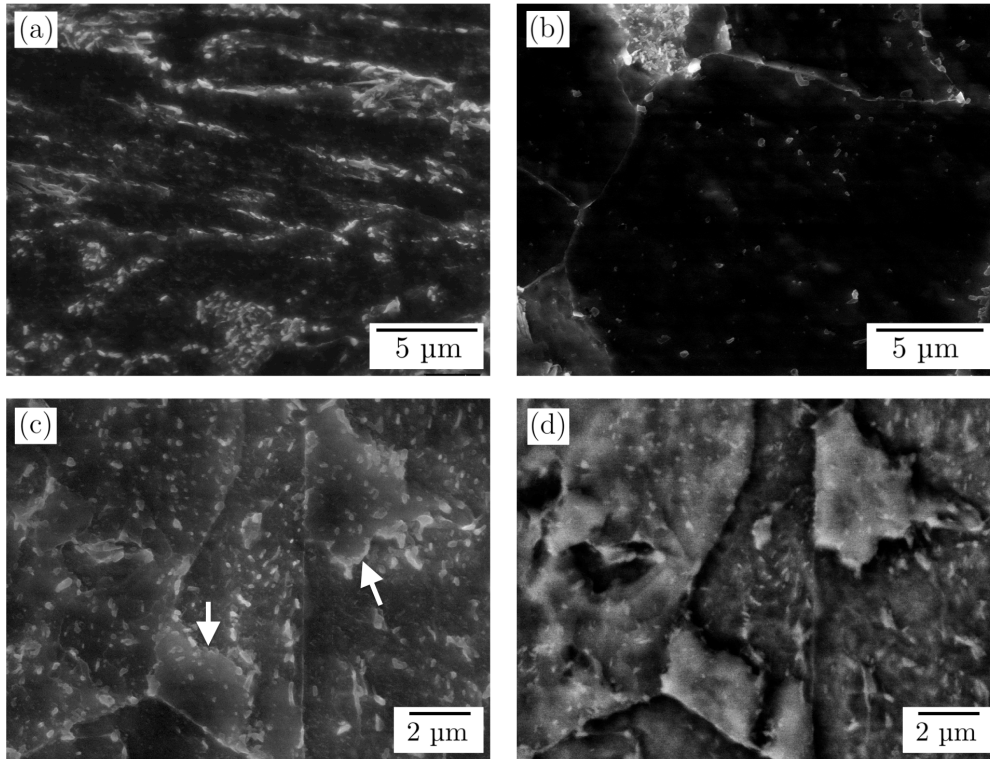


Figure 11: SEM images of tempered material in the etched condition. (a), (b) and (c) show secondary-electron images of the Widmanstätten bulk, allotriomorphic ferrite and enriched material respectively. Regions more resistant to etchant are highlighted in (c) and imaged with back-scattered electrons in (d).

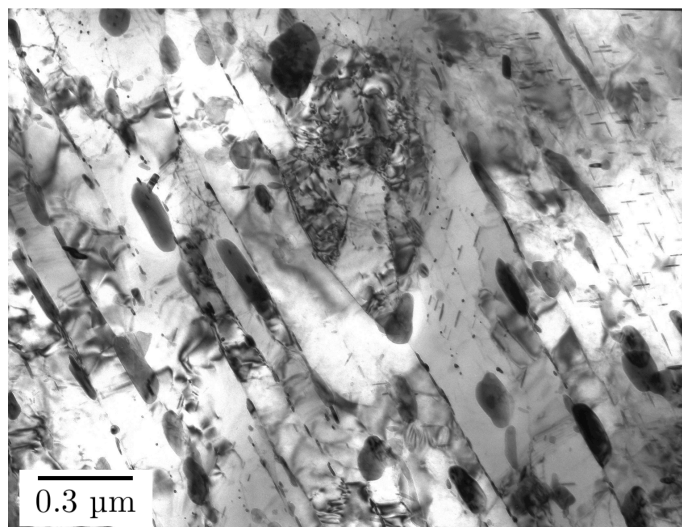


Figure 12: Tempered A-segregate material, showing coarse cementite carbides amongst fine bainite plates. Also present are fine needles of  $\text{Mo}_2\text{C}$ .

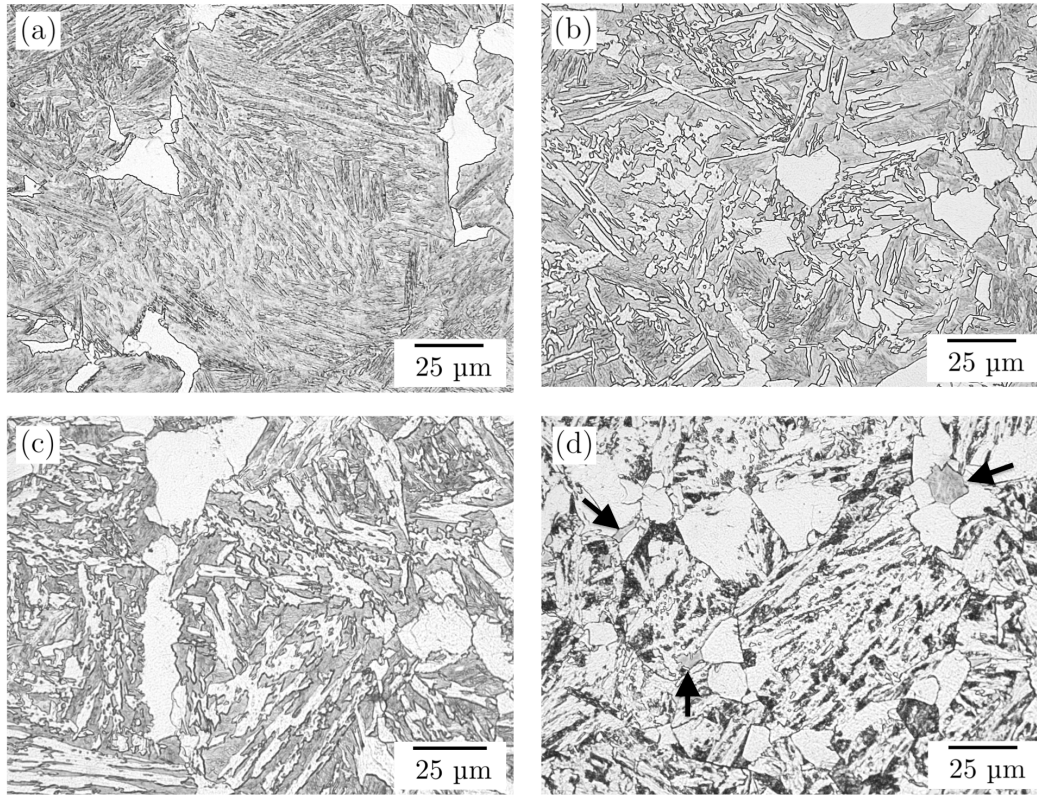


Figure 13: Partial-transformation experiments in material without A-segregation. (a)-(d) Microstructures when quenched at points A-D, respectively, in Fig. 4. Regions of untransformed material are indicated in (d).

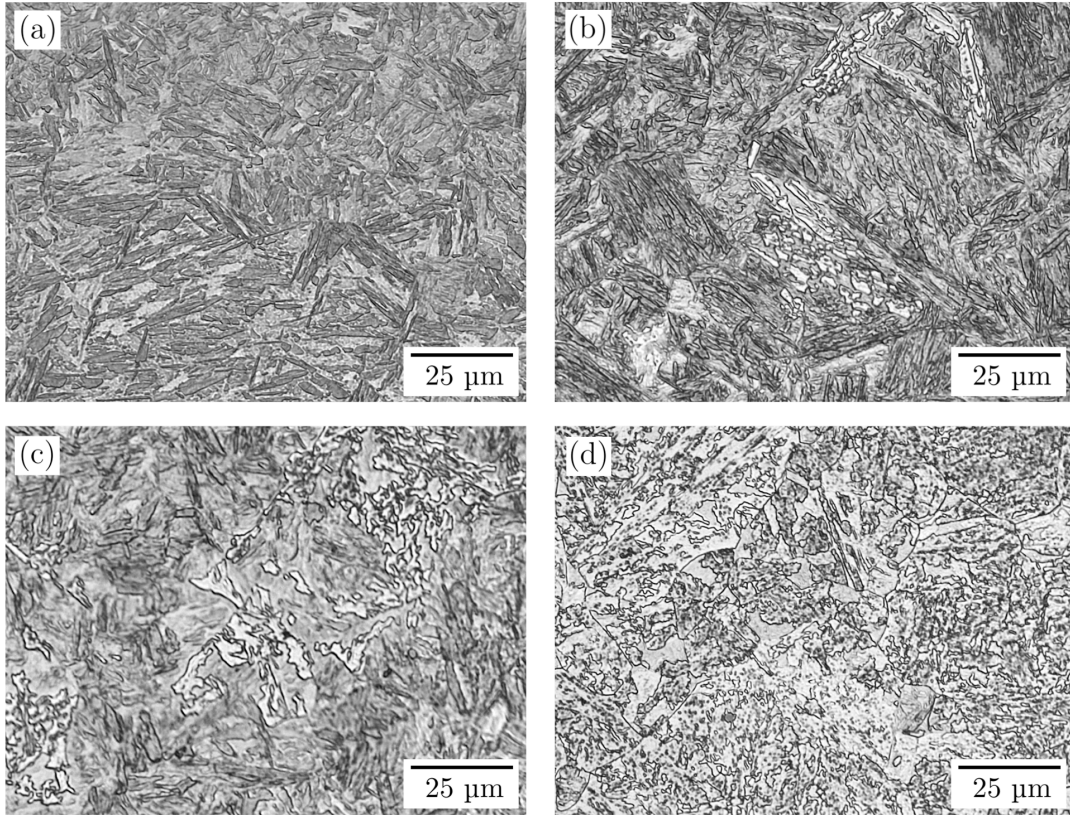


Figure 14: Partial-transformation experiments in material with A-segregation. (a)-(d) show microstructures when quenched at points equivalent to A-D (in enriched samples), respectively, in Fig. 4.

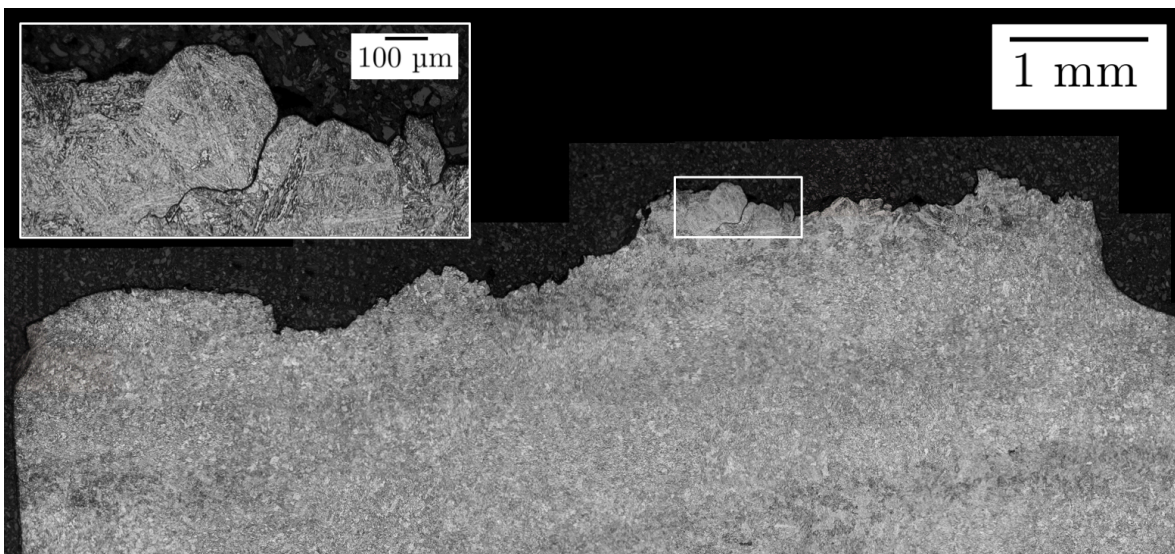
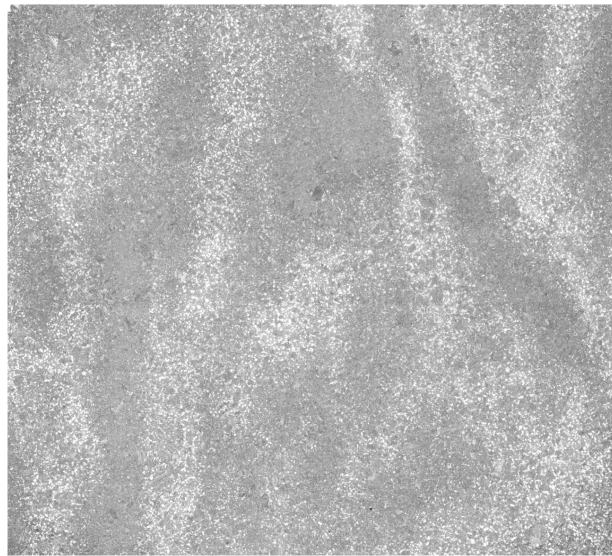


Figure 15: Intergranular failure in A-segregated material observed in a standard 10 x 10 x 55 mm Charpy impact test at  $-50^{\circ}\text{C}$ . The viewing plane is perpendicular to the crack surface, with the notch to the right of the image. This specimen was machined such that A-segregated material lay across the entire width of piece ahead of the notch.



1 mm

Figure 16: Depleted regions at the centres of prior dendrite arms, associated with bands of allotriomorphic ferrite; cf. point B in Fig. 4.

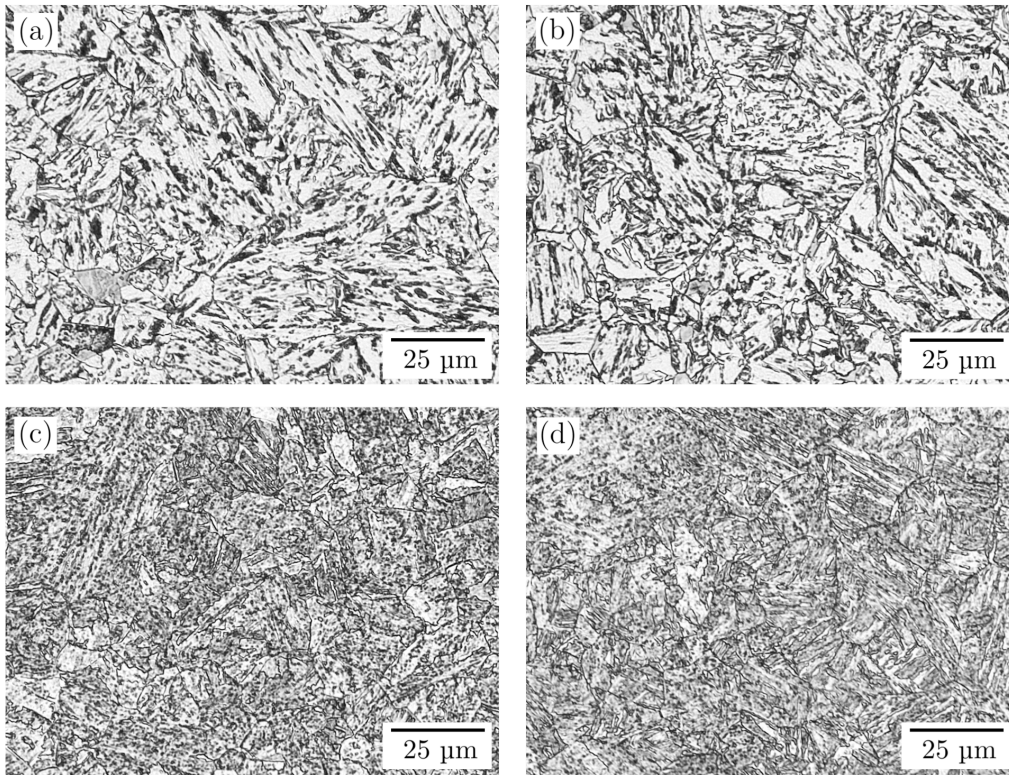


Figure 17: Optical micrographs of faster-quenching experiments. (a)  $0.2^{\circ}\text{C s}^{-1}$  in the bulk, (b)  $0.4^{\circ}\text{C s}^{-1}$  in the bulk, (c)  $0.2^{\circ}\text{C s}^{-1}$  in A-segregate and (d)  $0.4^{\circ}\text{C s}^{-1}$  in A-segregate.

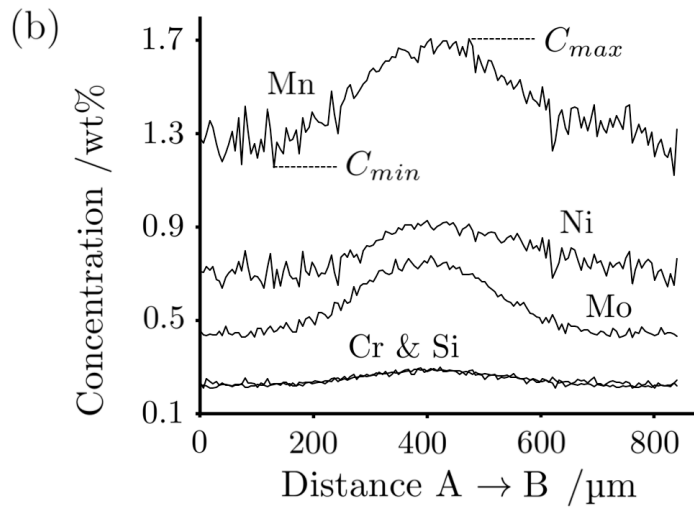
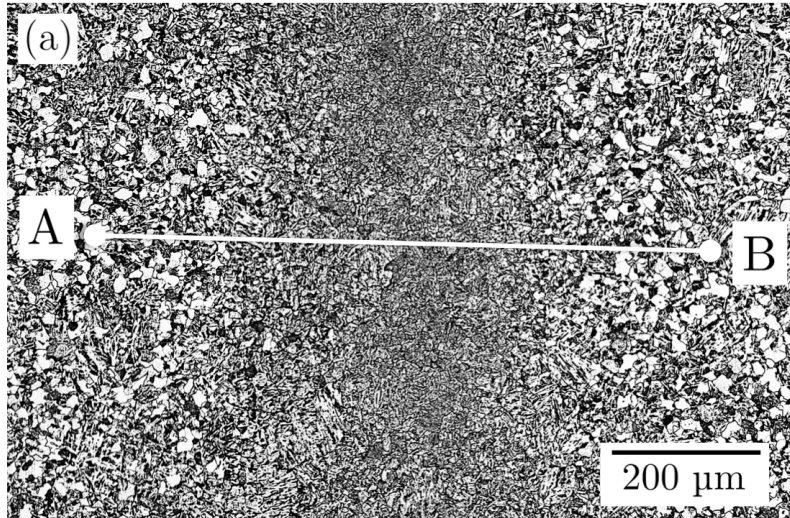


Figure 18: EPMA linescan results. (a). Optical micrograph of line analysed, which spanned the distance between two dendrite arms protruding into an A-segregate channel. (b). Plot showing variation in concentration of species, measured using EPMA with a step size of 5.2 μm and probe size of 1 μm.

**[Tables]**

Table 1: Composition (wt%) of SA508 Grade 3 steel examined.

Chemistry					
C	Mn	Ni	Mo	Si	Cr
0.184	1.317	0.736	0.488	0.253	0.212
Cu	Al	P	Sn	V	S
0.025	0.018	0.005	0.004	0.004	0.001

Table 2: Dilatometry data; the uncertainties are calculated from the standard deviation in a dataset of values for each sample type. The error in the ‘range’ combines that in the ‘onset’ and ‘end’ temperatures.

	With A-Segregate	Without A-Segregate
Ferrite onset /°C	676 ± 13	672 ± 8
Ferrite end /°C	639 ± 8	640 ± 5
Ferrite range /°C	37 ± 21	32 ± 13
% Ferrite (600°C)	12 ± 6	13 ± 3
Widmanstätten onset /°C	546 ± 10	553 ± 4
Widmanstätten end /°C	363 ± 14	380 ± 6
Widmanstätten range /°C	183 ± 24	173 ± 10
Martensite onset /°C	153 ± 5	153 ± 4

Table 3: EPMA broad-beam spot analysis (beam width 40 µm). Bold numbers are the composition in wt%, standard deviations are given in parentheses and the italicised figure is the value of  $C/C_0$  calculated using the concentrations in Table 1 as  $C_0$  values.

Region	Mn	Ni	Mo	Si	Cr
	<b>1.59</b>	<b>0.86</b>	<b>0.62</b>	<b>0.28</b>	<b>0.26</b>
A-Segregate	(0.07)	(0.04)	(0.06)	(0.01)	(0.01)
	<i>1.21</i>	<i>1.17</i>	<i>1.27</i>	<i>1.10</i>	<i>1.22</i>
Allotriomorphic ferrite	<b>1.26</b>	<b>0.69</b>	<b>0.45</b>	<b>0.24</b>	<b>0.22</b>
	(0.06)	(0.03)	(0.01)	(0.01)	(0.01)
	<i>0.96</i>	<i>0.93</i>	<i>0.93</i>	<i>0.94</i>	<i>1.04</i>
Widmanstätten ferrite	<b>1.28</b>	<b>0.69</b>	<b>0.47</b>	<b>0.24</b>	<b>0.22</b>
	(0.04)	(0.02)	(0.02)	(0.01)	(0.01)
	<i>0.97</i>	<i>0.94</i>	<i>0.95</i>	<i>0.94</i>	<i>1.05</i>

Table 4: Hardness measurements taken from three distinct microstructures found in material.  $\pm$  error in each result is one standard deviation.

Region	Hardness \ HV2	
	As-Quenched	Tempered
<b>A-Segregate</b>	318 $\pm$ 17	240 $\pm$ 17
<b>Allotriomorphic ferrite</b>	210 $\pm$ 15	181 $\pm$ 11
<b>Widmanstätten ferrite</b>	243 $\pm$ 10	200 $\pm$ 10

Table 5: Hardness measurements taken from the two distinct microstructures found in material quenched at faster rates.  $\pm$  error in each result is one standard deviation.

Region	Hardness \ HV2			
	0.2°C s <sup>-1</sup> Quench		0.4°C s <sup>-1</sup> Quench	
	As-Quenched	Tempered	As-Quenched	Tempered
<b>A-Segregate</b>	342 $\pm$ 32	252 $\pm$ 7	404 $\pm$ 29	258 $\pm$ 11
<b>Widmanstätten ferrite</b>	246 $\pm$ 10	198 $\pm$ 8	248 $\pm$ 8	198 $\pm$ 4

Table 6: Measured compositions of A-segregate and dendrite-arm material,  $C_{max}$  and  $C_{min}$ , which are referred to in Fig. 18. The results of MTDATA equilibrium (lever-rule) and Scheil solidification calculations are also shown, giving liquid concentrations when the fraction solid was 0.95.

	Concentration /w%				
	Mn	Ni	Mo	Si	Cr
$C_{max}$	1.71	0.92	0.78	0.29	0.30
$C_{min}$	1.16	0.64	0.43	0.21	0.21
$C_{Lever}^{f_s=0.95}$	1.78	0.77	0.90	0.40	0.25
$C_{Scheil}^{f_s=0.95}$	4.56	0.93	4.38	0.87	0.40